Unusual appearance of mother-of-pearl clouds above El Calafate, Argentina (50°21′S, 72°16′W)

Weather – December 2020, Vol. 75, No. 12

Andreas Dörnbrack[1], Bernd Kaifler[1], Natalie Kaifler[1], Markus Rapp[1], Norman Wildmann[1], Markus Garhammer[2], Klaus Ohlmann[3], James M. Payne[4], Morgan Sandercock[4] and Elizabeth J. Austin[4,5]

[1]*Institut für Physik der Atmosphäre, DLR Oberpfaffenhofen, Oberpfaffenhofen, Germany*
[2]*Meteorologisches Institut, Ludwig-Maximilians-Universität München, Munich, Germany*
[3]*Mountain Wave Project e. V, Grand Terrus, Montclus, France*
[4]*The Perlan Project, Inc, Beaverton, Oregon, USA*
[5]*WeatherExtreme Ltd, Incline Village, Nevada, USA*

Introduction

Perpetual strong surface winds are one of the distinctive features of Patagonia. At higher levels, these winds form clouds in amazingly weird shapes, covering the enormous sky in the lee of the Andes. As an occasional visitor, one wishes to sit there calm and serenely (surely in a wind shelter) and to watch the boundless shapes of clouds that form relentlessly and display themselves in an immense variation of shades.

However, on a field campaign, the reality looks slightly different. One watches the sky whenever the schedule allows. Here, we report on a lucky moment that occurred on the evening of 11 September 2019 in El Calafate, Argentina. While in the car, two single, well-separated mother-of-pearl clouds were spotted in the west over the Andes. These irradiant clouds (Figures 1 and 2) were reminiscent of the polar stratospheric clouds (PSCs) that have often been observed in the Arctic (Dörnbrack *et al*., 1999 and references therein). Usually, ice PSCs require stratospheric temperatures well below 190K, which are normally only attained inside the Antarctic polar vortex, but these clouds appeared far north of Antarctica, at nearly 50°S. Obviously, the unusual appearance of these clouds over El Calafate requires a scientific explanation.

Using different perspectives, the subsequent section presents observational evidence of the stratospheric clouds over Patagonia in early September 2019. The investigation of the meteorological situation reveals a direct association with the sudden warming in the southern hemispheric stratosphere occurring at this time. During this period, the polar vortex was shifted towards South America, and its cold pool was directly located above Patagonia. Using high-resolution (HRES) state-of-the-art NWP model data of the European Centre for Medium-Range Weather Forecasts (ECMWF), we outline the special meteorological situation and explain the circumstances under which the clouds had formed. Complementary numerical simulations corroborate the hypothesis of a singular mountain wave-induced PSC event. They also reveal that the atmospheric dynamics of this event are characterised by two main processes: first, the transience of the low-level forcing and propagation conditions and, second, the strong nonlinearity

Figure 1. Mother-of-pearl clouds west-southwest of El Calafate on 11 September 2019 at around 2300 UTC.

Figure 2. Mother-of-pearl clouds west-southwest of El Calafate on 11 September 2019. The picture was taken from outside the city at the cabins belonging to Brillos Patagónicos, Calle 78 750, El Calafate (50.32°S, 72.26°W) at around 2300 UTC. (Photo taken by Marko Magister, Big Air Factory.)

that is related to the breaking of the mountain waves in the middle stratosphere.

Observations

Visual observations from the ground

Figures 1 and 2 present photographs of mother-of-pearl clouds that were taken in El Calafate at around 0800h local time on 11 September 2019 (2300 UTC). On this day, strong surface winds prevailed, and wave-induced cirrus clouds had already appeared over the Lago Argentino in the morning (Figure 3). Mountain wave-like lenticular-shaped mother-of-pearl clouds were also seen in Rio Grande (53.78°S, 67.72°W, about 650km southeast of El Calafate) in the evening at around the same local time.

Visual observations in the stratosphere

The third deployment of the Airbus Perlan 2 mission[1] (Butler, 2016) occurred in August/September 2019 in El Calafate. The manned glider Perlan 2 was designed to fly up to 90 000ft (FL 900). During the 2019 deployment, several flights were conducted, reaching flight levels close to FL 500 (~15km altitude), with one flight attaining FL 650 (~19.3km on 16 September 2019). On 11 September 2019, Perlan 2 climbed up to FL 506 (15.2km altitude at around 1800 UTC). Before reaching the peak altitude, chief pilot Jim Payne spotted lenticular mother-of-pearl clouds in the stratosphere over the Andes at around 1730 UTC. Figure 4 juxtaposes two snapshots from the tail wing camera of Perlan 2 that display PSCs. Both photos were taken at nearly the same geographical location between 1719 and 1728 UTC. Obviously, the nearly 180° difference in the true headings of the glider indicates the existence of two spatially separated cloud groups, with one group located southwest and the other northwest from the aircraft location. The northern group did not seem to persist as long into the evening as the southern group. A short movie of Perlan 2 soaring in the stratosphere and recording the mother-of-pearl clouds in the northwest can be found on the Perlan project page[2]. The altitude and temperature profiles recorded by Perlan 2 and by a second instrumented glider, Stemme ST V10 (Wildmann *et al.*, 2020), operating in the troposphere at around the same time are shown in Appendix A. In summary, both the strong tropospheric and the lower stratospheric uplifts (vertical air velocity in excess of 5ms^{-1}) in the mountain lee waves generated favourable soaring conditions for both gliders that climbed up to 15km (Perlan 2) and to 8.8km (Stemme). Sensors on both aircrafts measured very low temperatures (~210K at 15km) at peak altitudes; see Appendix A.

Figure 3. Lee wave clouds above the Lago Argentino looking west, 11 September 2019, 0941 local time, 1241 UTC.

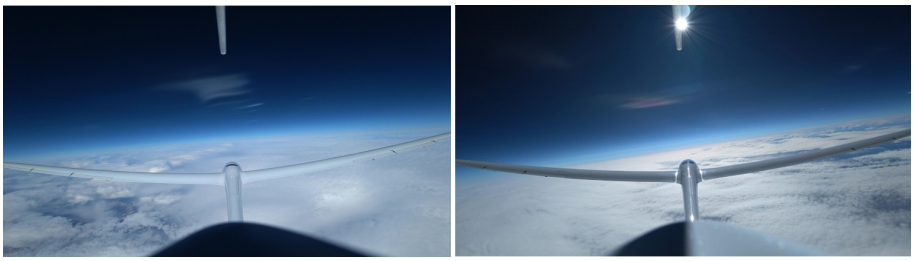

Figure 4. Snapshots of mother-of-pearl clouds from the camera installed on the Perlan 2 aircraft's tail wing. Left panel: position: 50.66°S, 73.04°W, altitude: 13 873m, true heading: 168.7°, time: 1728 UTC. Right panel: position: 50.59°S, 73.04°W, altitude: 14 933m, true heading: 347.4°, time: 1719 UTC.

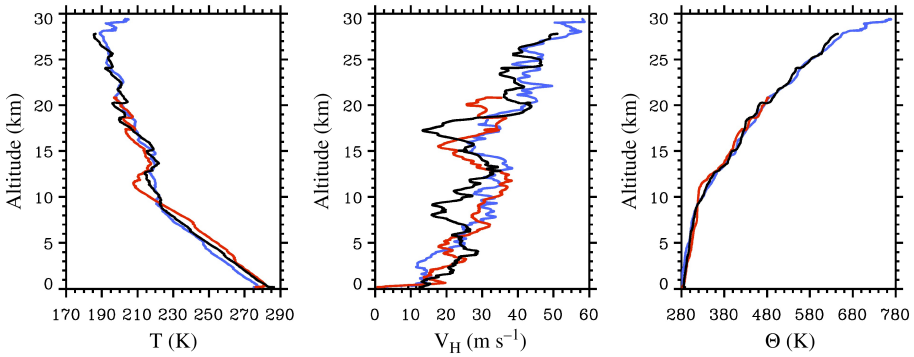

Figure 5. Vertical profiles of temperature T, horizontal wind V_H and potential temperature Θ measured by three soundings from El Calafate. Red and black lines: soundings from the iMet-4-AB (https://www.intermetsystems.com/ee/pdf/202084-11_iMet_Technical_Data_Sheet.pdf) radiosonde launched from the airport of El Calafate (50.51°S, 72.08°W) at 1057 UTC and 1703 UTC, respectively. Blue lines: sounding from Väisälä radiosonde RS41-SG (https://www.vaisala.com/de/products/instruments-sensors-and-other-measurement-devices/soundings-products/rs41) launched from El Calafate (50.32°S, 72.26°W) at 2355 UTC.

Radiosondes

Three soundings from El Calafate document the conditions in the lee of the Andes from 1100 UTC on 11 September 2019 until 0000 UTC on 12 September 2019; see Figure 5. The vertical temperature profiles reveal an increase of about 10K at mid-tropospheric levels during the 12-h period. The sharp tropopause at an altitude of about 11km in the 1100 UTC sounding disappeared in both the afternoon and evening soundings. Both changes are most likely related to the warm front passing through that day.

The stratospheric portion of the profiles is characterised by wave-like oscillations attaining amplitudes of about 10K. These layers appear in the three profiles at varying altitudes and are related to nearly neutrally stratified layers, leading to staircase-like profiles of potential temperature Θ, especially at altitudes of around 17km and above 20km. A comparison with the horizontal wind V_H appearing in these layers suggests that localised patches of decelerated flow appear in regions of wave overturning, where gravity waves extract momentum from the mean flow, for example, Durran (1995). Minimum temperatures of around 185K (–88°C) were measured at an altitude of about 27km.

Airborne LiDAR measurements

The German research aircraft HALO was based in Rio Grande, Tierra del Fuego,

[1]https://perlanproject.org/ and https://www.aerosociety.com/news/surfingthe-mountain-wave/.
[2]https://perlanproject.org/blog/perlan-2-soars-rare-stratosphericperlan-clouds.

to conduct research flights during the SOUTHTRAC mission (Southern hemisphere Transport, Dynamics, and Chemistry, see Rapp *et al*., 2020). On 11 September 2019, the HALO research flight ST08 took off in Rio Grande at 2305 UTC and headed northwest over the Andes, returning along nearly the same path. At around 2345 UTC and at 0115 UTC, the airborne Rayleigh LiDAR ALIMA (Airborne LIdar for Middle Atmosphere) measured enhanced backscatter between altitudes of 24 and 26km close to El Calafate (Figure 6).

The aerosol anomaly was calculated using the standard temperature retrieval of the Rayleigh measurements, assuming an aerosol-free atmosphere, that is, the backscatter profile measured by the LiDAR is proportional to air density (pure Rayleigh scattering). Here, atmospheric density is inferred from the measured photon count profiles. The actual temperature profiles, T(z), are computed by top–down integrations, assuming hydrostatic equilibrium (Hauchecorne and Chanin, 1980), and by using observed Microwave Limb Sounder (MLS, on NASA's Earth Observing System Aura) temperatures at around 95km as starting values. Atmospheric layers with enhanced aerosol loads generate extreme low temperatures in this computation. By defining a reference temperature T_{ref}, the normalised difference $(T_{ref} - T(z))/T_{ref}$ defines the aerosol anomaly displayed in Figure 6. The value of T_{ref} = 176K has been selected as the minimum nightly mean temperature minus 10K in this altitude band, measured by the ground-based LiDAR system Compact autonomous Rayleigh Lidar (CORAL), located in Rio Grande in September 2018 (Kaifler *et al*., 2020). The reference temperature T_{ref} affects the calculated aerosol anomalies linearly. A lower (higher) T_{ref} value leads to smaller (larger) aerosol anomalies. The actual minimum temperature on the day of the flight is not known; however, the selected low T_{ref} value provides a very high probability that the actual lowest stratospheric temperature is higher. In that sense, T_{ref} = 176K represents a conservative estimate, and eventually, layers of enhanced aerosol loads can be unambiguously assigned to altitudes with $T(z) < T_{ref}$.

The shape of the aerosol anomaly, marked with arrows in Figure 6, resembles lenticular mountain wave-induced PSCs, and it is very likely that they are the mother-of-pearl clouds as seen in El Calafate (Figures 1 and 2) and from the Perlan 2 aircraft (Figure 4). During the 90min between the first and second underpass, the PSC signal fades due to the weakening of the low-level forcing that is studied in the section 'High-resolution numerical simulations'.

It is interesting to note that aerosol anomalies are also present south of 54°S along the path of the research flight ST08, indicating the presence of widespread PSCs (Figure 6). These PSCs are located at lower altitudes inside the cold pool of the Antarctic polar vortex; see next section.

It must be noted that the observed PSCs are optically thin. For the stronger aerosol anomalies south of El Calafate, a maximum backscatter ratio of 1.03 was determined. This is a rather low value compared to typical measurements of Arctic PSCs, with values up to 1.2, and supports our finding of the very faint appearance of the mother-of-pearl clouds near El Calafate. A further classification or determination of particle sizes, colour ratio, etc. is, unfortunately, not possible as the Rayleigh LiDAR has no other wavelengths or depolarisation channels to permit such calculations. Nevertheless, the exact determination of the altitude of the PSCs is possible. The very low temperatures, $T < 190$K, as measured by the two radiosondes support the existence of ice particles (Figure 5). However, one has to remember that these radiosonde observations were conducted more than 100km downstream of El Calafate, and the ALIMA observations were directly above the Andes, about 85km southwest of El Calafate.

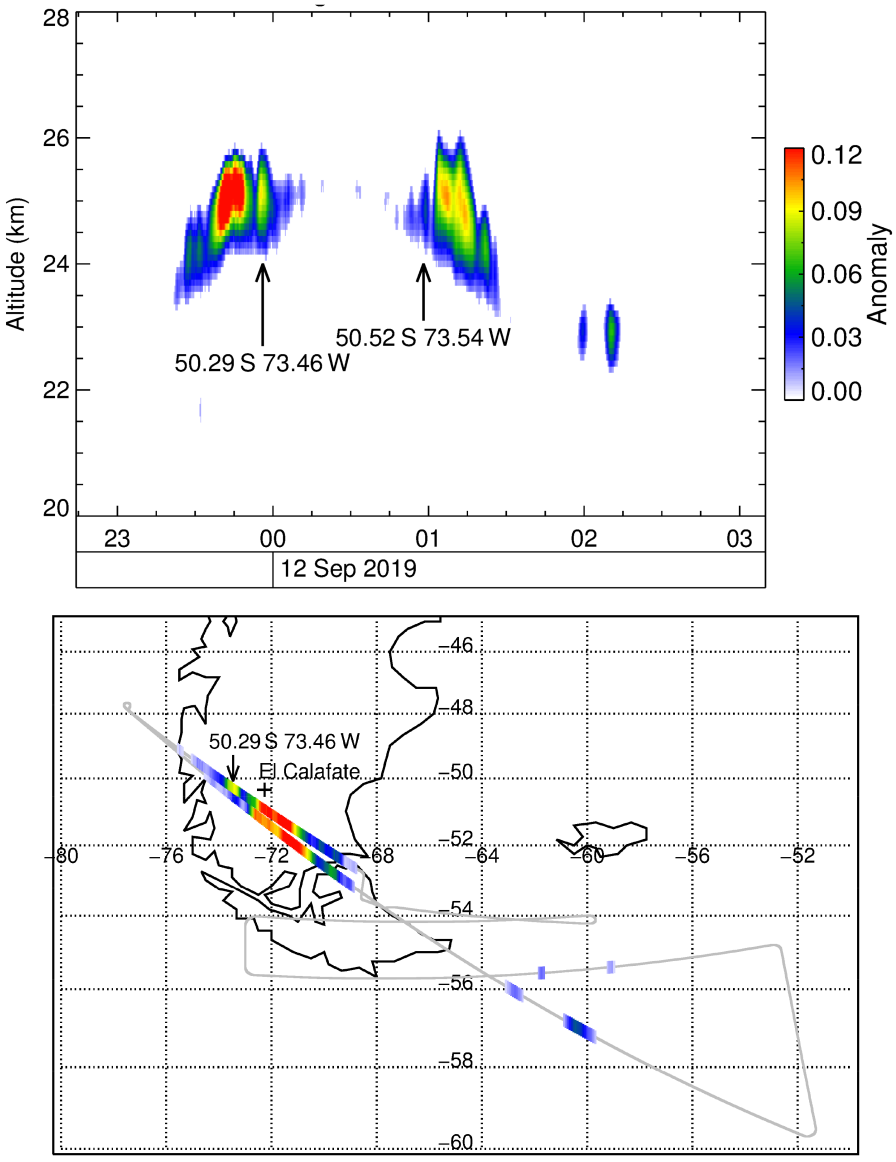

Figure 6. Aerosol anomaly (for definition, see text) calculated from ALIMA temperature profiles along the whole flight track of HALO ST08 from 11 September 2019 at 2305 UTC until 12 September 2019 at 0721 UTC. Top: vertical section, bottom: vertically integrated aerosol anomaly.

Atmospheric conditions during the austral winter 2019

The southern polar vortex in late austral winter of 2019 broke down early due to a sudden stratospheric warming (SSW). According to classic metrics, it was a minor SSW, but it appeared as a major event as it changed the propagation conditions for mountain waves markedly in September 2019 (Rapp *et al*., 2020). Figure 7 shows the temporal evolution of the zonal mean zonal wind around 60°S, both at 1hPa and at 10hPa, for the 3 years 2002, 2006 and 2019.

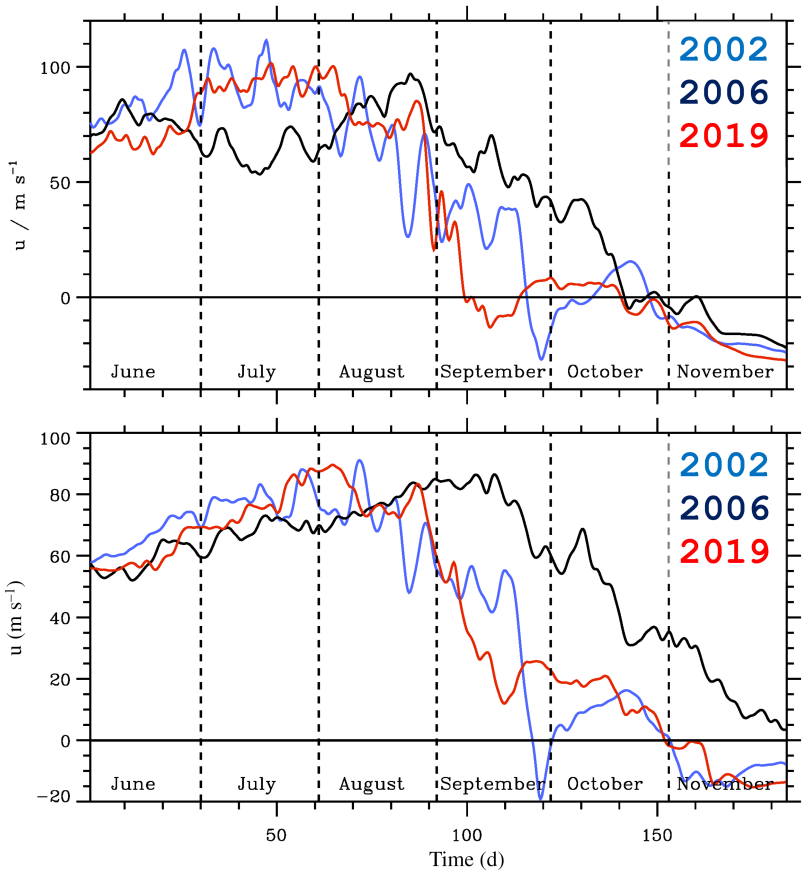

Figure 7. Zonal mean zonal winds averaged between 55°S and 65°S at 1hPa (top panel) and 10hPa (lower panel) for the years 2002, 2006 and 2019. (Source data for ERA5 analyses: Hersbach et al., 2020.)

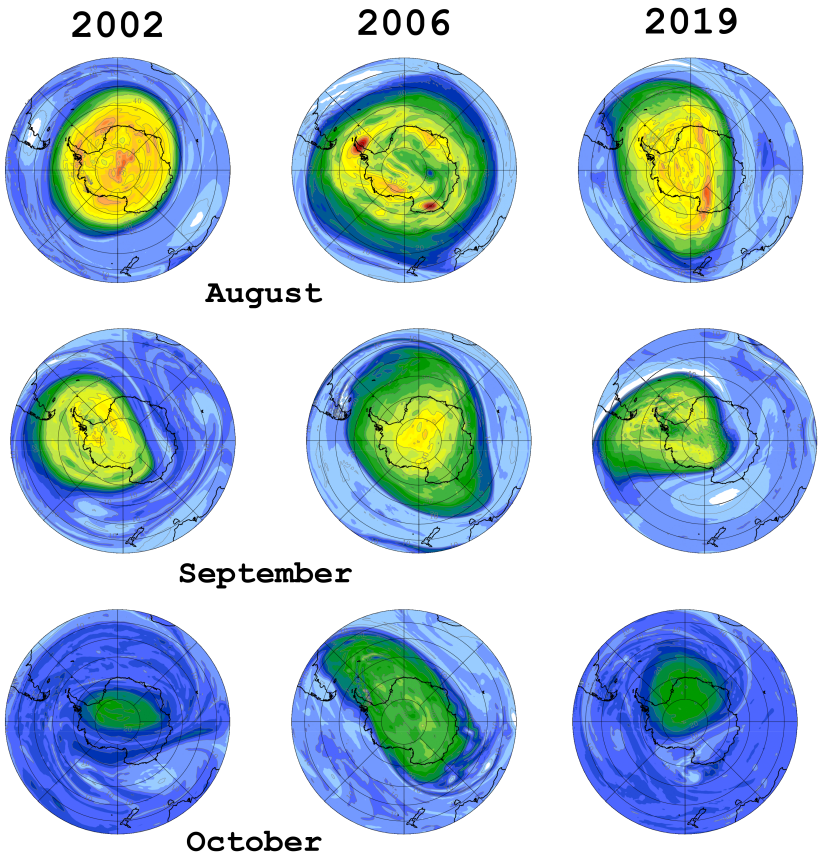

Figure 8. Scaled potential vorticity at the 850K isentropic surface on the 11th of each of the months of August, September and October at 1200 UTC for the years 2002, 2006 and 2019. (Source data: ERA5 analyses.)

The year 2002 is an extraordinary year when the only reported major SSW occurred in the Southern Hemisphere (Krüger *et al.*, 2005); 2006, in contrast, has been considered an average year in a climatological sense (see figure 4 in Byrne and Shepherd, 2018). The evolution of the year 2019 was anomalous in that the wind, at 1hPa, reversed quite early in the season. However, the wind anomaly did not penetrate down to the 10hPa level. Therefore, the sudden warming of 2019 cannot be classified as a major SSW (Yamazaki *et al.*, 2020). However, one clearly sees that the wind reversal in atmospheric layers above 10hPa lasted until the final breakdown of the southern hemispheric vortex.

Figure 8 juxtaposes the scaled potential vorticity at the 850K stratospheric isentropic surface on the 11th of each of the months of August, September and October for the 3 years. Already in August 2019, the vortex was offset slightly from the pole compared to the previous years, and its shape became more elongated. The disturbance became striking in September 2019, when the vortex area shrunk and the centre was displaced towards South America. This transition is similar to the evolution in 2002 and differs markedly from 2006. Finally, in October 2019, the shape, strength and position of the polar vortex were very similar to those in 2002, whereas the vortex was stronger and larger in 2006.

Mountain wave-induced temperature anomalies

Operational HRES analyses of the EMCWF's Integrated Forecast System (IFS) are used to visualise the hemispheric temperature field at 20hPa (~25km altitude) on 11 September 2019 at 1800 UTC and 12 September 2019 at 0000 UTC, Figure 9. The cold pool of the polar vortex is displaced from its dynamical centre, located at about 80°S and 45°W over Antarctica. This shift indicates strong baroclinicity during the ongoing SSW. Minimum temperatures emerge over the southern tip of South America. They appear in elongated streaks associated with undulations in the geopotential height field and are related to the mountain waves resolved in the IFS (Dörnbrack *et al.*, 2017). Elongated, coherent regions of negative or positive temperature anomalies, T', are denoted as phase lines of the mountain waves. The resolved temperature fluctuations, T', are shown in Figure 10 for a section over South America. At the 20hPa level, T' attains peak-to-peak amplitudes of a maximum of 20K. The ambient temperature is reduced by about 10K directly over the Andes to the west of El Calafate. These mountain wave-induced stratospheric temperature anomalies first appeared in the IFS analyses at 1200 UTC

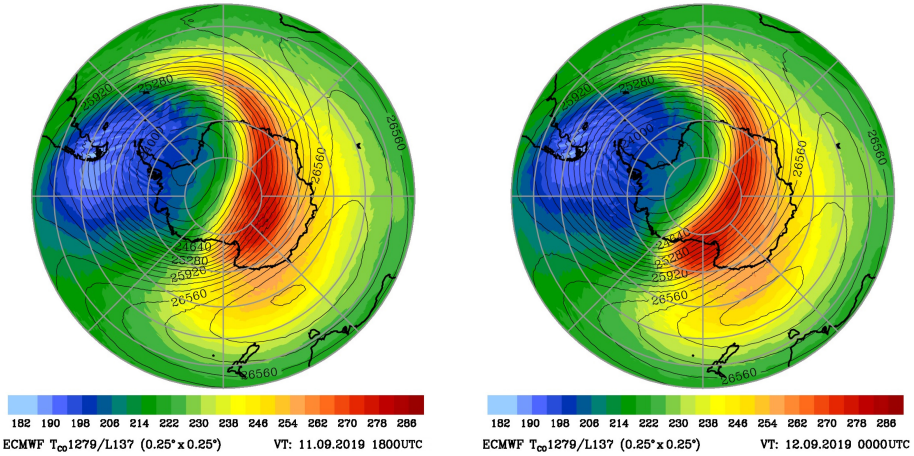

Figure 9. Absolute temperature and geopotential height at the 20hPa pressure level on 11 September 2019 at 1800 UTC (left panel) and 12 September 2019 at 0000 UTC. (Source data: IFS operational analyses.)

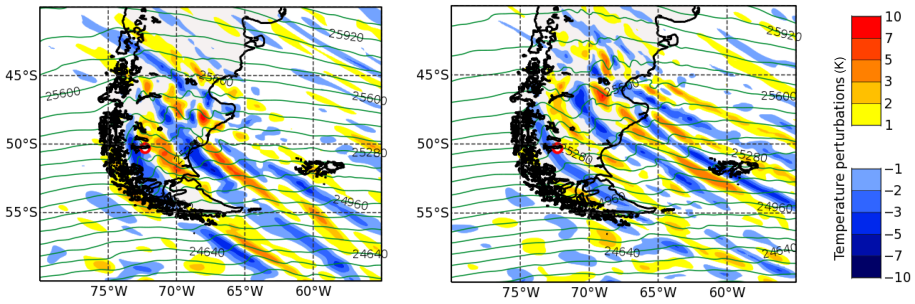

Figure 10. Temperature perturbation $T' = T_{1279} - T_{106}$ (K, colour shaded) geopotential height (m, green lines) at the 20hPa pressure level and 11 September 2019 at 1800 UTC (left panel) and 12 September 2019 at 0000 UTC. The red encircled symbol marks the location of El Calafate, Argentina. (Source data: IFS operational analyses.)

on 11 September 2019 and remained there until 0000 UTC, after which they gradually disappeared, a time period that fits well with the observations presented above. The phase lines of the mountain waves extend in an approximate bow shape towards the southeast. This process is related to the horizontal dispersion of the quasi-steady hydrostatic gravity waves (Gill, 1982; Smith, 1989). Here, the waves propagate meridionally into the core of the polar night jet that is located to the south of El Calafate, a dynamical process well described, for example, by Preusse *et al*. (2002) and Sato *et al*. (2012) and further discussed by Ehard *et al*. (2017) and Jiang *et al*. (2019) for New Zealand.

Two sets of vertical sections complete the analysis by means of the IFS. Figure 11 displays the temperature perturbations, T', associated with the mountain waves along 50.25°S, the latitude of El Calafate, and 50.5°S on 11 September 2019 at 1200 and 1800 UTC. The mountain waves present themselves as alternating positive and negative T' values with increasing amplitudes in the stratosphere. As indicated above, the mountain waves are nearly stationary, and only the phases of the T' anomalies propagate gradually upwards in time, possibly related to the transient upstream conditions; see next section. The sections at both latitudes show a singular stratospheric region, where the local temperatures fall below the existence temperature of ice clouds, T_{ice}. The shape and the altitude of this ice cloud resemble those

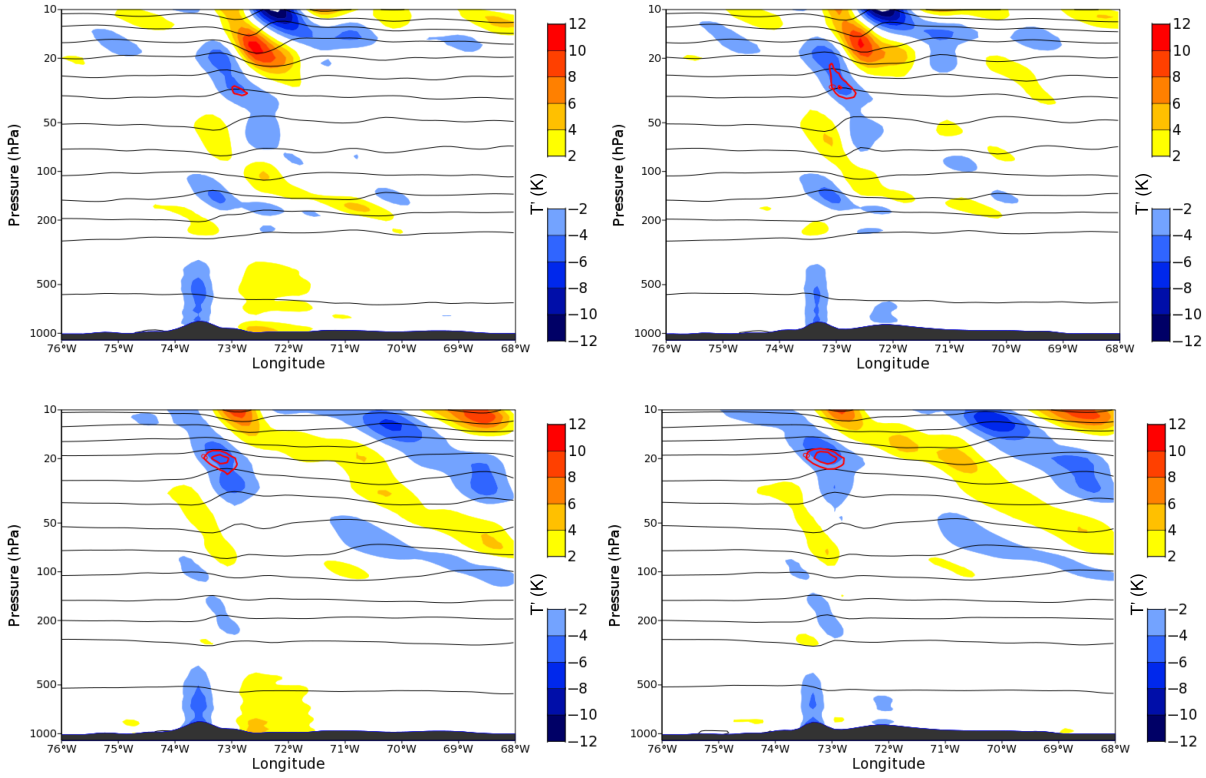

Figure 11. Temperature perturbation $T' = T_{1279} - T_{106}$ (K, colour shaded), $\Delta T_{ice} = -1K$ and 0K (red contour lines, see text) and logarithm of Θ (increment 0.075) at 50.25°S (left) and 50.50°S (right) on 11 September 2019 at 1200 UTC (top row) and 1800 UTC (bottom row). (Source data: IFS operational analyses.)

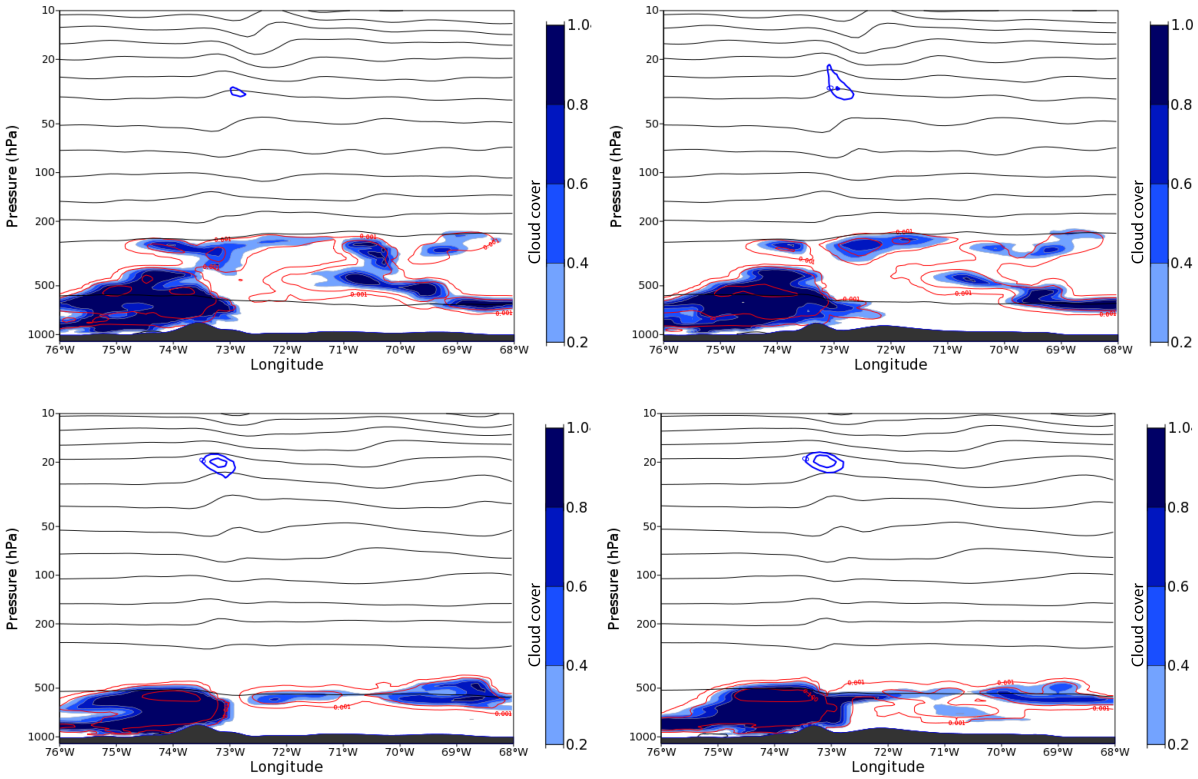

Figure 12. Cloud cover (blue shaded), cloud ice water content (gkg^{-1}, red contour lines), $\Delta T_{ice} = -1$K and 0K (blue contour lines, see text) and logarithm of Θ (increment 0.075) at 50.25°S (left) and 50.50°S (right) on 11 September 2019 at 1200 UTC (top row) and 1800 UTC (bottom row). (Source data: IFS operational analyses.)

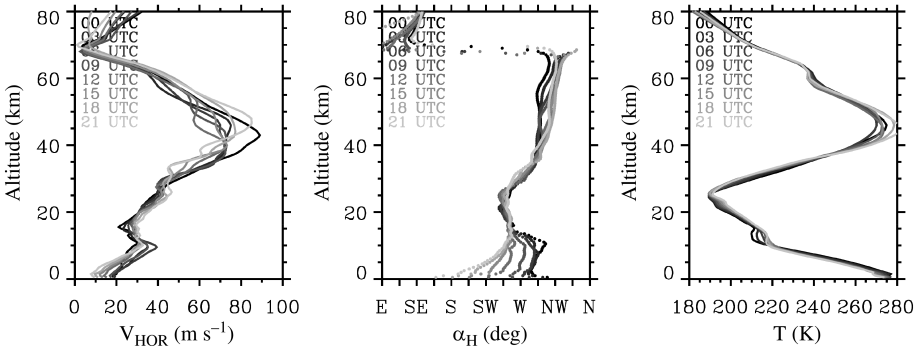

Figure 13. Upstream profiles of the horizontal wind V_{HOR}, the wind direction α_H and the absolute temperature T for 11 September 2019. The individual profiles are averages in an area between 77.5°W and 82.5°W and 47.5°S and 52.5°S. (Source data: ERA5 analyses.)

of the visual and airborne LiDAR observations. The plotted values of $\Delta T_{ice} = T - T_{ice}$ are calculated using the ice frost point formula of Marti and Mauersberger (1993). Modified IFS values of the water vapour mixing ratio q_{H_2O} from the IFS are used: In order to show the principal possibility of the existence of a stratospheric ice cloud, and taking into account the uncertainty of analysed stratospheric q_{H_2O} values, we enhanced q_{H_2O} by 2ppmv (parts per million by volume as the specific humidity q_{H_2O} was converted to a volume mixing ratio). A similar effect can be achieved by decreasing the local temperature because smaller-scale, high-frequency internal gravity waves as those observed cannot be resolved by the operational IFS data offering a horizontal resolution of about 9km (Podglajen *et al.*, 2020).

Figure 12 presents the tropospheric clouds as well as the stratospheric ice cloud analysed by IFS. The simulated cloud structures very closely resemble the observations from this day. Thin, high ice clouds (Figure 3) were replaced by lower-level clouds related to the warm front that occurred later during this day (not shown). The characteristic low-level upstream blocking is well represented by the dense tropospheric clouds in the IFS analyses.

High-resolution numerical simulations

Two-dimensional numerical simulations were conducted by EULAG (see Appendix B for the equations solved numerically and the set-up) to figure out if a higher resolved topography might produce larger temperature amplitudes in the mountain waves. We also investigate the impact of upstream conditions on the wave-induced temperature amplitudes by using 3-hourly initial times t_{INIT} from 0600 UTC until 2100 UTC.

Figure 13 displays individual vertical profiles of the horizontal wind V_{HOR}, the wind direction α_H and the absolute temperature T computed in a box covering the upstream area from 77.5°W to 82.5°W and 47.5°S to 52.5°S from 0000 to 2100 UTC on 11 September 2019. The lower tropospheric wind V_{HOR} decreased from 20ms^{-1} to about 10ms^{-1} from 0000 UTC to 2100 UTC. During the same period, the wind direction α_H turned from northwesterly to southerly in the troposphere. This means that the low-level forcing (which is essentially proportional to the normal wind component of the main mountain ridge of the Andes, i.e. the zonal wind) peaked at around 0900 to 1200 UTC and was weaker before and after. There are modulations in V_{HOR} and α_H at stratospheric levels that are related to the large-scale change of the ambient state due to the SSW. The impact of the SSW can be seen in the wind reversal at altitudes greater than 70km. Based on upstream profiles, the propagation conditions for gravity waves changed only marginally in the stratosphere during the whole period. However, this does not consider the drastic change of profiles above and to the lee of the Andes due to the vertically propagating mountain waves.

The simulated mountain wave-induced temperature fluctuations $T' = T - T_e$ are shown in Figure 14 after 1 and 2 hours

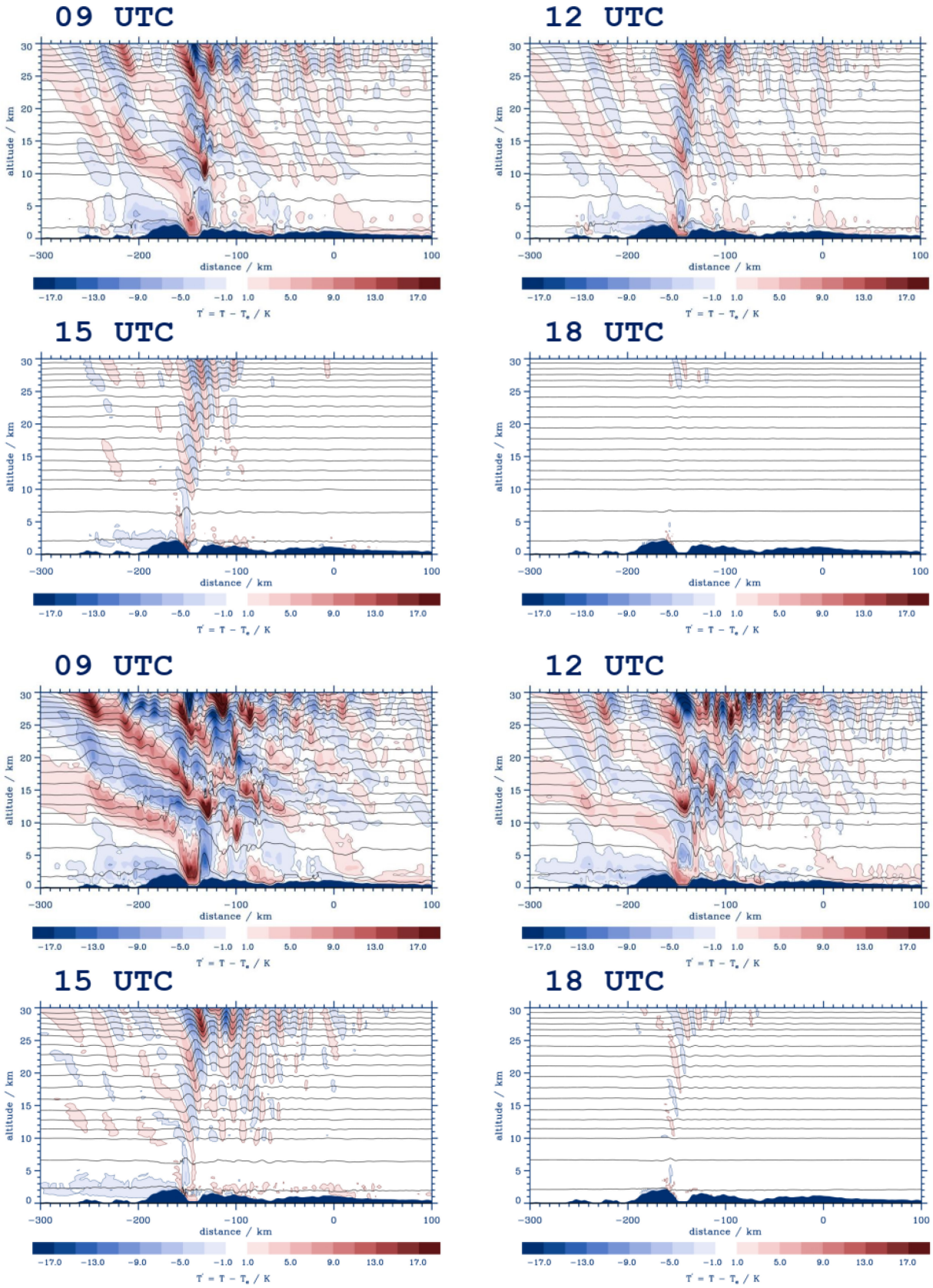

Figure 14. (a) Temperature fluctuations $T - T_e$ (colour shaded, K) after 1 hour simulation time from four EULAG simulations starting on 11 September 2019 at the given times. The orography is shown at latitude $\varphi = 50°S$. (b) Temperature fluctuations $T - T_e$ (colour shaded, K) after 2h simulation time from four EULAG simulations starting on 11 September 2019 at the given times. The orography is shown at latitude $\varphi = 50°S$.

simulation times. The four panels relate to different times of initialisation (t_{INIT} = 0900, 1200, 1500 and 1800 UTC), and ambient temperature profiles $T_e(z)$ correspond to the different initial profiles and do not change in time during the simulation. After a simulation time of 1 hour, all simulations show vertically propagating mountain waves. The T' amplitudes are largest for the 0900 and 1200 UTC runs, and they are nearly zero for the simulation starting at 1800 UTC, reflecting the reduced low-level forcing at this time. At an altitude of about 25km, T' falls below −10K. After a simulation time of 2 hours, the numerical simulations ini-

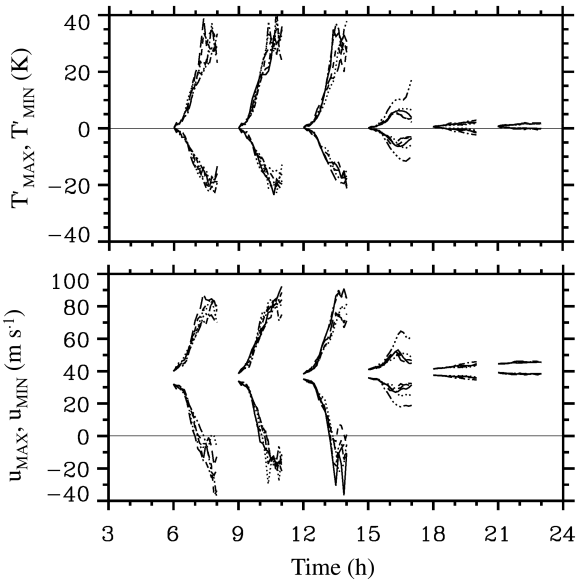

Figure 15. Top panel: Minimum and maximum temperature fluctuations $T' = T - T_e$ as function of time and computed in a box from $-200\text{km} < x < -50\text{km}$ and $22.5\text{km} < z < 27.5\text{km}$ (x denotes the distance and z the altitude as shown in Figure 14) for 30 numerical integrations starting at t_{INIT} = 0600, 0900, 1200, 1500, 1800 and 2100 UTC on 11 September 2019. Bottom panel: the same as for the top panel but for minimum and maximum zonal wind. The different line styles refer to the different latitudes for which the simulations were conducted. Solid, dotted, dashed, dash-dot and dash-dot-dot-dot lines refer to φ = 50°S, 50.25°S, 50.50°S, 50.75°S and 51°S, respectively.

tialised at 0900 and 1200 UTC show strong nonlinearities, resulting in the overturning of isentropic surfaces due to breaking mountain waves. The simulations using the later initialisation times t_{INIT} remain nearly linear in the stratosphere due to the weaker low-level forcing. Amplitudes of T' are maximised, and T' attains values less than −10K. This means the stratospheric temperatures can be reduced by more than 10K due to the adiabatic cooling in the ascending branches of the mountain waves. Given an ambient $T \sim 195$K, local temperature below 185K can be expected at an altitude of around 25km.

The temporal evolutions of the minimum and maximum T' values are shown in Figure 15 for all 30 numerical integrations. The particular values are computed in a box from $-200\text{km} < x < -50\text{km}$ and $22.5\text{km} < z < 27.5\text{km}$, where x denotes the distance in streamwise direction and z the altitude; see Figure 14. In addition, the evolution of the minimum and maximum zonal winds are displayed in Figure 15. The magnitude of the T' values increases in time for all simulations, whereby the runs for $t_{INIT} > 1500$ UTC reveal a drastic reduction of the T' magnitude compared to the earlier initialisation times. This behaviour is in accordance with the weaker low-level forcing. These earlier simulations (t_{INIT} = 0600, 0900, 1200 UTC) produce extreme T' amplitudes of nearly 40K. However, one has to consider that these values are simulated at a stage when the mountain waves break. The onset of wave breaking inside the considered box is indicated by the local flow reversal, that is, when u_{MIN} drops below zero in Figure 15. In almost all cases, the onset of nonlinear wave breaking occurs after a simulation time of 3600s. This means that the extremely large T' amplitudes cannot be considered realistic as the actual nonlinear breaking process can only be simulated by using three spatial dimensions, a task that will be tackled in the future.

Conclusions

The combination of tropospheric and stratospheric visual observations of mother-of-pearl clouds with airborne remote-sensing measurements and temperature profiles from nearby radiosonde soundings shows evidence of mountain wave-induced PSCs forming in the ascending branches of the gravity wave. The altitude of the PSCs was between 25 and 26km. Minimum stratospheric temperatures at these altitudes were below 185K and allowed for the existence of ice clouds. It must be noted that, in 2 years of continuous ground-based LiDAR measurements since November 2017, no PSCs have been detected by CORAL in Rio Grande. This finding confirms the peculiarity of the observed mother-of-pearl clouds in September 2019 during the early minor SSW and the associated displacement of the Antarctic polar vortex.

The location and altitude of the ice PSCs are extremely well predicted by the HRES operational analyses of the ECMWF's IFS. A set of 2-dimensional numerical simulations confirms the dominating hydrostatic character of the mountain waves, leading to a localised cooling of more than 10K compared to the ambient upstream profiles. Moreover, these simulations highlight the strong nonlinearity and transience of the stratospheric wave dynamics. This means that the 2-dimensional simulations fail to reproduce the real wave dynamics under such transient forcing conditions as soon as wave breaking, reflection and refraction, as well as the generation of secondary waves, become important. The difficulties arising from the transience of the low-level forcing are discussed in Portele *et al*. (2018). Altogether, the simulation and interpretation of nonlinear wave dynamics above and in the lee of the Andes are big challenges.

Acknowledgments

This paper was written when the first author was a guest at the Finnish Meteorological Institute (FMI) in Sodankylä, Finland. AD thanks Rigel Kivi and all the colleagues from FMI for their enduring support in the crazy times of March 2020. We thank the staff of El Calafate airport and Empresa Argentina de Navegación (EANA) for facilitating the glider flights from the airport in El Calafate and in the Argentinian airspace. We especially thank Patrick and Sandra who hosted the motor glider pilots, the film team and DLR/LMU staff at the Brillos Patagónicos cabañas. They allowed us to launch radiosondes from there and provided sustained support for many professional and personal issues. This research was partly funded by the Deutsche Forschungsgemeinschaft (DFG) via the project MS-GWaves (GW-TP/DO 1020/9-1, PACOG/RA 1400/6-1). Access to ECMWF data was granted through the special project 'Deep Vertical Propagation of Internal Gravity Waves'.

Data availability statement

The Perlan 2 data (Excel data from flight no. 63 and the two radiosonde soundings from El Calafate airport) are downloaded from the Perlan project page http://www.perlan-project.cloud/data. The free accessibility of these data is greatly appreciated. The ALIMA data, as well as the radiosonde from El Calafate, are available from the HALO database (https://halo-db.pa.op.dlr.de). ECMWF ERA5 data are available via the ECMWF web page https://www.ecmwf.int/en/forecasts/datasets/reanalysis-datasets/era5.

References

Amante C, **Eakins BW**. 2009. ETOPO1 1 arc-minute global relief model: procedures, data sources and analysis, in *NOAA Technical Memorandum NESDIS NGDC-24*. National Geophysical Data Center, NOAA: Boulder, CO.

Butler D. 2016. Surfing glider set to study climate. *Nature* **536**: 134–135.

Byrne NJ, **Shepherd TG**. 2018. Seasonal persistence of circulation anomalies in the Southern Hemisphere stratosphere and its implications for the troposphere. *J. Climate* **31**: 3467–3483.

Dörnbrack A, **Leutbecher M**, **Kivi R** ***et al***. 1999. Mountain-wave-induced record low stratospheric temperatures above northern Scandinavia. *Tellus A* **51**: 951–963.

Dörnbrack A, **Gisinger S**, **Pitts MC** ***et al***. 2017. Multilevel cloud structures over Svalbard. *Mon. Weather Rev.* **145**: 1149–1159.

Durran DR. 1995. Do breaking mountain waves decelerate the local mean flow? *J. Atmos. Sci.* **52**: 4010–4032.

Ehard B, **Kaifler B**, **Dörnbrack A** ***et al***. 2017. Horizontal propagation of large-amplitude mountain waves into the polar night jet. *J. Geophys. Res.* **122**: 1423–1436.

Gill AE. 1982. *Atmosphere-Ocean Dynamics*, 1st Edition. Academic Press: New York, NY.

Hauchecorne A, **Chanin ML**. 1980. Density and temperature profiles obtained by lidar between 35 and 70 km. *Geophys. Res. Lett.* **7**: 565–568.

Hersbach H, **Bell B**, **Berrisford P** ***et al***. 2020. The ERA5 global reanalysis. *Q. J. R. Meteorol. Soc.* **146**: 1999–2049.

Jiang Q, **Doyle JD**, **Eckermann SD** ***et al***. 2019. Stratospheric trailing gravity waves from New Zealand. *J. Atmos. Sci.* **76**: 1565–1586.

Kaifler N, **Kaifler B**, **Dörnbrack A** ***et al***. 2020. Lidar observations of large-amplitude mountain waves in the stratosphere above Tierra del Fuego, Argentina. *Sci. Rep.* **10**: 14529

Krüger K, **Naujokat B**, **Labitzke K**. 2005. The unusual midwinter warming in the Southern Hemisphere stratosphere 2002: a comparison to Northern Hemisphere phenomena. *J. Atmos. Sci.* **62**: 603–613.

Kühnlein C, **Smolarkiewicz PK**, **Dörnbrack A**. 2012. Modelling atmospheric flows with adaptive moving meshes. *J. Comput. Phys.* **231**: 2741–2763.

Leutbecher M, **Volkert H**. 2000. The propagation of mountain waves into the stratosphere: quantitative evaluation of three-dimensional simulations. *J. Atmos. Sci.* **57**: 3090–3108.

Marti J, **Mauersberger K**. 1993. A survey and new measurements of ice vapor pressure at temperatures between 170 and 250 K. *Geophys. Res. Lett.* **20**: 363–366.

Podglajen A, **Hertzog A**, **Plougonven R** ***et al***. 2020. Lagrangian gravity wave spectra in the lower stratosphere of current (re)analyses. *Atmos. Chem. Phys.* **20**: 9331–9350.

Portele TC, **Dörnbrack A**, **Wagner JS** ***et al***. 2018. Mountain-wave propagation under transient tropospheric forcing: a DEEPWAVE case study. *Mon. Weather Rev.* **146**: 1861–1888.

Preusse P, **Dörnbrack A**, **Eckermann SD** ***et al***. 2002. Space-based measurements of stratospheric mountain waves by CRISTA 1. Sensitivity, analysis method, and a case study. *J. Geophys. Res.* **107**(D23): 8178

Prusa JM, **Smolarkiewicz PK**. 2003. An all-scale anelastic model for geophysical flows: dynamic grid deformation. *J. Comput. Phys.* **190**: 601–622.

Prusa JM, **Smolarkiewicz PK**, **Garcia RR**. 1996. Propagation and breaking at high altitudes of gravity waves excited by tropospheric forcing. *J. Atmos. Sci.* **53**: 2186–2216.

Prusa JM, **Smolarkiewicz PK**, **Wyszogrodzki AA**. 2008. EULAG, a computational model for multiscale flows. *Comput. Fluids* **37**: 1193–1207.

Rapp M, **Kaifler B**, **Dörnbrack A** ***et al***. 2020. SOUTHTRAC-GW: an airborne field campaign to explore gravity wave dynamics at the world's strongest hotspot. *Bull. Am. Meteorol. Soc.* (under review)

Sato K, **Tateno S**, **Watanabe S** ***et al***. 2012. Gravity wave characteristics in the Southern Hemisphere revealed by a high-resolution middle-atmosphere general circulation model. *J. Atmos. Sci.* **69**: 1378–1396.

Smith RB. 1989. Hydrostatic flow over mountains. *Adv. Geophys.* **31**: 1–41.

Smolarkiewicz PK, **Kühnlein C**, **Wedi NP**. 2014. A consistent framework for discrete integrations of soundproof and compressible PDEs of atmospheric dynamics. *J. Comput. Phys.* **263**: 185–205.

Wildmann N, **Eckert R**, **Dörnbrack A**. 2020. In-situ measurements of wind and turbulence by a motor glider in the Andes. *J. Atmos. Ocean. Technol.* (under review)

Yamazaki Y, **Matthias V**, **Miyoshi Y** ***et al***. 2020. September 2019 Antarctic sudden stratospheric warming: quasi-6-day wave burst and ionospheric effects. *Geophys. Res. Lett.* **47**: e2019GL086577

Correspondence to: A. Dörnbrack

andreas.doernbrack@dlr.de

doi: 10.1002/wea.3863

Appendix A: Glider measurements

Two gliders were operated around El Calafate on 11 September 2019. The Airbus Perlan 2 conducted the flight no. 63. During this flight, a peak altitude of FL 506 (~15.2km altitude at around 1800 UTC = 64 800s) was attained. Perlan 2 was towed up to an altitude of about 14km and reached the 15km mark three times (Figure A1, left panel). The locations of the maximum altitudes are marked in the track plot of Figure A1, right panel.

The second aircraft was a motor glider of type Stemme S10 VT (Wildmann *et al.*, 2020). It climbed, motorised, up to about 1.5km, and after switching off the engine, the glider sunk to an altitude of 1km. Thereafter, the Stemme soared in the waves up to an altitude of 8.8km (Figure A1, left panel). Due to the extremely low air temperature (Figure A2, left panel), unfortunately, the data logger switched off, and only wind and temperature data from the first part of the flight are available. Also, the Perlan 2 aircraft encountered very low stratospheric temperatures of around 210 to 220K at the highest flight levels.

The strength of the mountain waves can be estimated by the climb rates both aircraft experienced in the lee of the Andes, Figure A2 (right panel). The climb rate was calculated by central-differencing the 1s global positioning system (GPS) altitude data and filtering them with a 60s window. Although the pilots decided differently and soared either north (Stemme) or south (Perlan 2) of El Calafate, both aircrafts ascended up to 7ms^{-1} in some portions of the flights. Assuming aircraft sink rates of 0.8ms^{-1} (Stemme) and about 2ms^{-1} (Perlan 2), this translates to vertical winds reaching up to 5–7ms^{-1}. The measurements of the gust probe mounted on the Stemme confirm this estimate in parts for the tropospheric portion of the leeward mountain wave system, see Figure A3.

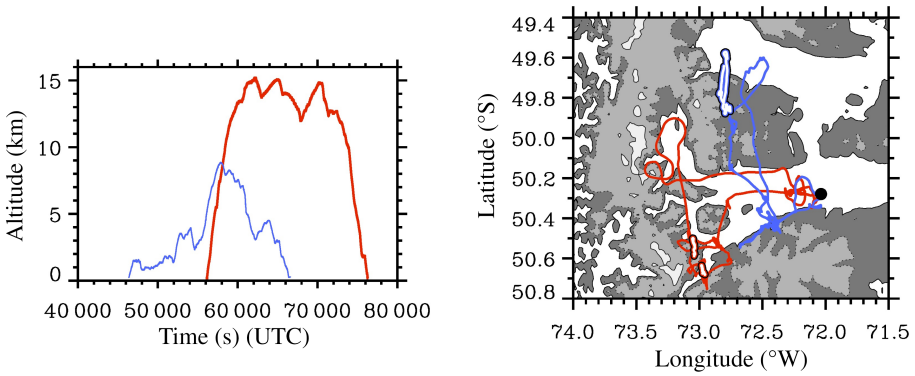

Figure A1. Altitude–time plot (left panel) and positions (right panel) of the two gliders operating on 11 September 2019 near El Calafate, Argentina (marked by the black dot). Red: Perlan 2 and blue: Stemme. The regions where Perlan 2 was above an altitude of 15km and the Stemme was above an altitude of 8km are marked with black-encircled white symbols in the right panel. The orography is shaded from dark to light grey at 500m, 1000m, 2000m and 3000m levels.

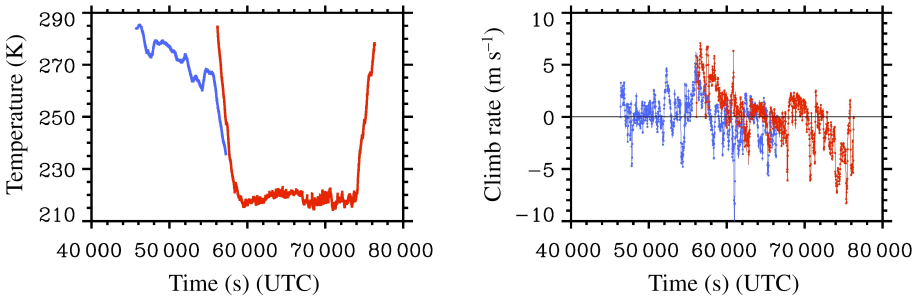

Figure A2. Absolute temperature (left panel) and climb rate (right panel) of the two gliders operating on 11 September 2019 near El Calafate. Red: Perlan 2 and blue: Stemme.

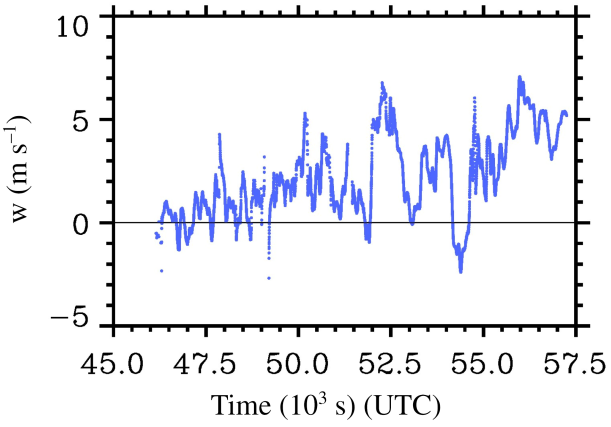

Figure A3. Vertical wind velocity component measured by the Stemme aircraft on 11 September 2019 near El Calafate.

Appendix B: The geophysical flow solver EULAG

The simulations for this paper were conducted with the multi-scale geophysical flow solver EULAG (Prusa *et al*., 2008; Smolarkiewicz *et al*., 2014). Here, the compressible Euler equations are:

$$\frac{\mathrm{d}\mathbf{u}}{\mathrm{d}t} = -c_P\theta\nabla\pi' - \boldsymbol{g}\frac{\theta'}{\theta_e} - f\times\left(u - \frac{\theta}{\theta_e}\mathbf{u}_e.\right)$$

$$\frac{\mathrm{d}\theta'}{\mathrm{d}t} = -\mathbf{u}\cdot\nabla\theta_e$$

$$\frac{\mathrm{d}\rho}{\mathrm{d}t} = -\rho\nabla\cdot\mathbf{u}$$

$$\pi = \left(\frac{R_d}{p_0}\rho\theta\right)^{R_d/c_v}$$

where $c_v = c_p - R_d$. In the above equations, the physical quantities have their usual meanings; primed quantities denote deviations to ambient states symbolised by subscript 'e'. Although we solve for the Cartesian velocity $\mathbf{u} = (u, v, w)$, the operators d/dt, ∇, $\nabla\cdot$ are formulated in generalised terrain-following coordinates (Prusa and Smolarkiewicz, 2003; Kühnlein *et al*., 2012). The above equations are integrated numerically as described by Smolarkiewicz *et al*. (2014).

The computational domain extends 1260km eastwards starting at 80°W, and the model top is at an altitude of 80km. The horizontal and vertical resolutions amount to 1km and 500m, respectively. The digital orography of the Andes along selected latitudes, φ = 50°S, 50.25°S, 50.50°S, 50.75°S, and 51°S, is taken from ETOPO1 global relief model (Amante and Eakins, 2009) and interpolated onto the regular 1km grid.

The lower boundary is a material surface, and we apply a free-slip boundary condition. As the main focus of the EULAG simulations was on the mountain wave response in the middle atmosphere, we do not resolve the surface boundary layer. Using realistic values for the surface roughness results in weaker stratospheric wave amplitudes, as shown by Leutbecher and Volkert (2000), but also requires a finer vertical resolution of the boundary layer. At the lateral edges of the computational domain, open boundary conditions are imposed. In addition, absorbing layers attenuate the flow variables toward their ambient states and avoid the reflection of waves into the computational domain. The sponge layers are 120km wide, and a relaxation time scale of 180s was chosen. At the free-slip model top, w = 0, and we use a z-dependent relaxation in the whole domain, mimicking the increasing dynamic viscosity with altitude, a method introduced by Prusa *et al*. (1996, section 3b). This particular choice of a vertical sponge avoids the reflection of gravity waves from the model top.

Background and initial fields are obtained from the ERA5 dataset (Hersbach *et al*., 2020). Vertical profiles of V_{HOR}, α_H and T are computed in an upstream box covering the areas from 77.5°W to 82.5°W and 47.5°S to 52.5°S from 0600 to 2100 UTC on 11 September 2019, see Figure 13. Simulations were performed using these ambient profiles as initial conditions in the whole domain.